

Patterning Hierarchy in Direct and Inverse Opal Crystals

Lidiya Mishchenko, Benjamin Hatton, Mathias Kolle, and Joanna Aizenberg*

Biological strategies for bottom-up synthesis of inorganic crystalline and amorphous materials within topographic templates have recently become an attractive approach for fabricating complex synthetic structures. Inspired by these strategies, herein the synthesis of multi-layered, hierarchical inverse colloidal crystal films formed directly on topographically patterned substrates via evaporative deposition, or “co-assembly”, of polymeric spheres with a silicate sol–gel precursor solution and subsequent removal of the colloidal template, is described. The response of this growing composite colloid–silica system to artificially imposed 3D spatial constraints of various geometries is systematically studied, and compared with that of direct colloidal crystal assembly on the same template. Substrates designed with arrays of rectangular, triangular, and hexagonal prisms and cylinders are shown to control crystallographic domain nucleation and orientation of the direct and inverse opals. With this bottom-up topographical approach, it is demonstrated that the system can be manipulated to either form large patterned single crystals, or crystals with a fine-tuned extent of disorder, and to nucleate distinct colloidal domains of a defined size, location, and orientation in a wide range of length-scales. The resulting ordered, quasi-ordered, and disordered colloidal crystal films show distinct optical properties. Therefore, this method provides a means of controlling bottom-up synthesis of complex, hierarchical direct and inverse opal structures designed for altering optical properties and increased functionality.

1. Introduction

Biological systems provide numerous examples of complex, micropatterned, inorganic single-crystalline or amorphous materials that grow within organic templates.^[1] Inspired by this strategy, the materials community has explored topographical templating as a synthetic technique for controlling

bottom-up growth of crystalline materials, their defect distribution and patterning, with the growth of single crystalline calcite structures around 2D and 3D patterned surfaces being the most prominent example.^[2] Topographical templating has also been coupled with other bottom-up material fabrication techniques, providing a cost-effective route for the self-assembly of hierarchical structures.^[3] Most notably, surface topography has been used to study and control the orientation and defect formation in colloidal crystal assembly.^[4]

Colloidal crystals are useful not only as model systems for studying atomically-scaled phenomena (defect formation in metals,^[5] phase transitions,^[6] etc.) at a larger scale, but also for bottom-up fabrication of complex materials for applications in optics,^[7] sensors,^[8] and data storage.^[9] These applications require the use of large-area (centimeter-scale), crack-free colloidal crystal films. However, growing large-scale colloidal crystals (so-called, direct opals) from suspension using various established techniques of self-assembly has posed a significant challenge, resulting in films with cracks,

L. Mishchenko, Dr. B. Hatton, Dr. M. Kolle,
Prof. J. Aizenberg
School of Engineering and Applied Sciences
Harvard University
29 Oxford St., Room 229, Cambridge, MA 02138, USA
E-mail: jaiz@seas.harvard.edu

Dr. B. Hatton, Prof. J. Aizenberg
Wyss Institute for Biologically Inspired Engineering
Harvard University
Cambridge, MA 02138, USA

DOI: 10.1002/smll.201102691



domain boundaries, and other defects;^[10] thus limiting their technological potential. In an attempt to gain more control over the assembly process, the first topographical templating technique, “colloidal epitaxy”, was demonstrated by sedimenting colloidal spheres onto a pattern of holes matching the crystal lattice spacing.^[11] In more recent, meniscus-driven (flow/evaporation) systems, raised pillar structures were found to manipulate the crystal stacking of deposited colloidal films.^[12] 2D and 3D colloidal crystals were also grown into channels to control crystal size, shape, and packing.^[13]

Colloidal crystals can be used as sacrificial templates for synthesizing porous inverse opal structures that have a unique range of advantageous properties. The interconnected highly-porous construction of inverse opals is useful in a wide range of fields, including photonics,^[14] tissue engineering,^[15] sensing,^[16] and catalysis.^[17] The synthesis of inverse opal materials typically involves the infiltration of a matrix material around a colloidal template *after* its self-assembly^[14d,18] and the subsequent removal of this template. This method has been applied for various inverse opal materials (e.g., SiO₂, TiO₂, and Al₂O₃), using solution sol–gel precursors such as metal alkoxides,^[19] the infiltration of nanoparticles,^[20] or deposition from a vapor phase.^[21] Unfortunately, these conventionally fabricated inverse opals inherit all the defects of their original colloidal crystal templates. They also develop additional defects due to under- or over-infiltration of the liquid precursor into the template and the high capillary forces associated with this infiltration, causing either structural collapse and cracking, or overlayer formation.^[18b] For the formation of inverse opal films by infiltration, it is generally difficult to achieve structural uniformity over length scales beyond ~50 μm. Moreover, complex inverse opal structures, in which controlled hierarchy and 3D defect distribution are used to manipulate light propagation,^[22] have been only realized using top-down patterning techniques. Since conventional inverse opals have to be made by infiltrating a direct opal template with a matrix material, this approach cannot be applied for bottom-up topographical templating of inverse opals and the analysis of their resulting changes in properties.

Recently we have demonstrated that multilayered, nano-composite colloidal crystal films can be generated via evaporative deposition by a “co-assembly” of polymeric colloidal spheres with a silicate sol–gel precursor solution.^[23] Removal of the colloidal template (i.e., thermal decomposition) produces inverse opal films with minimal cracking and large, centimeter-scale domains. In contrast to direct opals (colloids only), the simultaneous formation and association of the colloidal crystal and the polymerizing sol–gel network during co-assembly allows for the relaxation of tensile stresses encountered during the drying process necessary for crystallization. The ability to create large-scale, high-quality inverse colloidal crystal films greatly expands the real-world applications of these materials. We have also shown that the colloidal co-assembly method may provide a means for direct synthesis of inverse opals on topographically patterned substrates.^[23]

In order to extend the co-assembly method to create complex, hierarchical inverse opal structures with increased functionality, it is necessary to systematically study the response

of this system to artificially-imposed 3D topographical constraints, and to compare the resulting crystal quality to that of a direct opal grown on the same templates. However, the mechanisms of domain nucleation and the choice of crystallographic orientation in the growing crystals have yet to be fully understood in either system. A comprehensive understanding of the crystal growth orientation and the direction of crack propagation is still under debate even in better studied direct opals, with experiments suggesting that the domain orientation may depend on the crystal growth rate^[24] or the shape of the meniscus.^[25] Co-assembled opal composite structures are more of a mystery. Our previous work^[23] has shown that these crystals have a preferred <110> orientation with respect to the growth direction. We also observed that the co-assembled silica–colloid system possesses a self-correcting property that allows the crystal to regain its preferred <110> orientation even if a random nucleation source (i.e., dust particle) on the substrate forces the crystal to temporarily nucleate a differently-oriented crystal domain. Thus, comparing crystal growth of direct and co-assembled opals around deliberately imposed spatial constraints might lend some insight into domain nucleation and orientation in both colloidal systems.

Herein, colloidal crystals with and without a silica precursor—forming inverse and direct opals, respectively—were evaporatively assembled onto flat substrates and onto surfaces patterned with an array of features of various geometries (i.e., rectangular, triangular and hexagonal prisms and cylinders). These artificially imposed structures were rationally designed as 3D spatial constraints to control crystallographic domain nucleation and orientation. With this bottom-up topographical approach, we were able to nucleate distinct colloidal domains of a defined size, location and orientation in a wide range of length-scales, tune the degree of disorder in the crystal, and manipulate the optical properties of these films.

2. Results

2.1. Nucleation of Altered Domains

Polymeric colloids 450 nm in diameter were initially evaporatively deposited onto unpatterned silicon substrates from an aqueous solution to create direct opals (**Figure 1a**) and from a solution containing a silica precursor (hydrolyzed tetraethyl orthosilicate) for inverse opal fabrication (**Figure 1b**). **Figure 1a** shows a schematic of evaporative assembly of direct opals and typical images of actual films. The analysis of the SEM images and Fast Fourier Transforms (FFT) clearly reveal the formation of multiple domains that are differently oriented with respect to one another (**Figure 1a** inset and cropped FFT), with no well-defined growth orientation. (Note: All figures show films with growth direction pointing down towards the bottom of the page.) **Figure 1b** shows a schematic of co-assembly and SEM images of actual films after the colloidal template has been thermally removed.^[23] The resulting films are highly ordered and have a preferred <110> domain orientation with respect to the growth direction (see insets and FFT in **Figure 1B**).

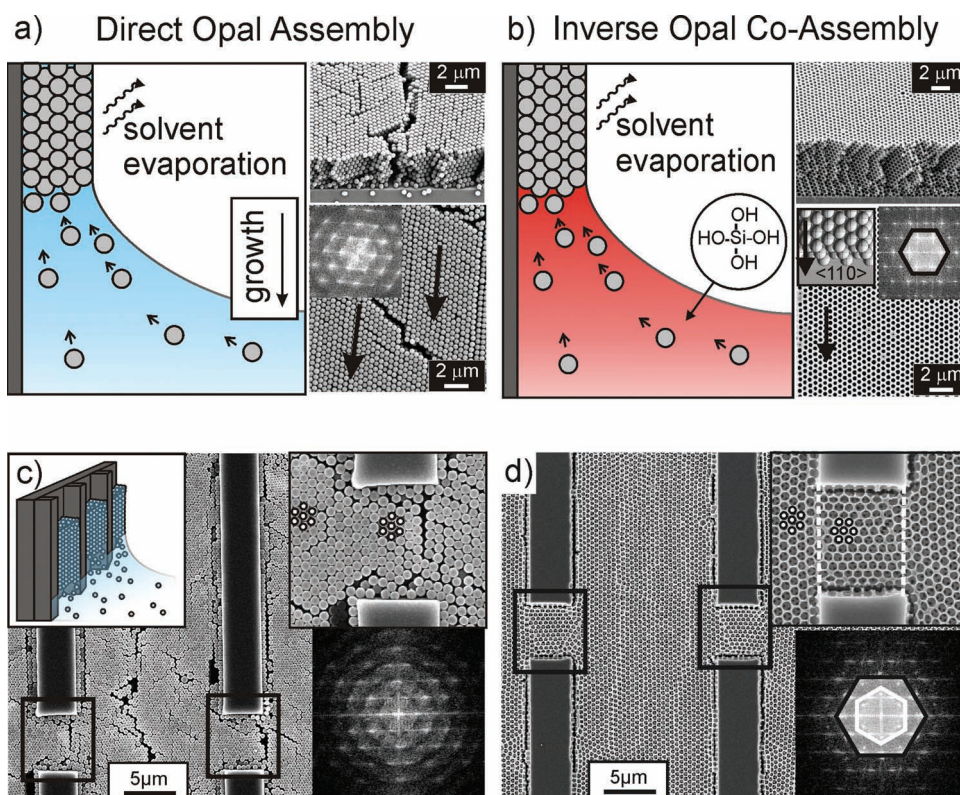


Figure 1. Comparison of direct (left) and inverse (right) opal assembly of 450 nm colloids on flat and patterned substrates. Note: All figures show films with growth direction pointing down towards the bottom of the page. a) Schematic (left) and scanning electron microscopy (SEM) images (right) of direct opal films assembled onto unpatterned substrates. Note the formation of domains of various crystallographic directions and cracking (see SEM images and FFT). Arrows indicate the $\langle 110 \rangle$ direction of domains. b) Schematic (left) and SEM images (right, after template removal) of inverse opals synthesized via co-assembly (incorporating a sol-gel silica precursor). The films have uniform domain orientation and no cracking over large areas (inset SEM images and FFT). The preferred growth direction ($\langle 110 \rangle$) is shown as a schematic in the inset (FFT and black hexagon emphasize the corresponding crystallographic orientation). c,d) SEM images of direct colloidal crystals (c) and inverse opal films (d) assembled on a substrate bearing an array of $1.5\text{ }\mu\text{m}$ -high \times $40\text{ }\mu\text{m}$ -long \times $4\text{ }\mu\text{m}$ -wide blades. Black boxes, white circles, and dashed white lines added for clarity. Schematic of the assembly process is shown in the inset on the left. c) Direct opals show no response to the wall orientation and form a disordered film (see FFT) similar to that shown in (a). d) Inverse opals form crystals grown in two orientations ($\langle 110 \rangle$ and $\langle 100 \rangle$) in response to a change in the blade wall orientation. The FFT shows the two crystallographic orientations (black and white hexagons).

As an initial test of how these two systems respond to imposed spatial constraints, direct and inverse opal films were grown into an all-silicon structure of patterned rectangular prisms (“blades”), $1.5\text{ }\mu\text{m}$ -high \times $40\text{ }\mu\text{m}$ -long \times $4\text{ }\mu\text{m}$ -wide in size, oriented along the film growth direction (Figure 1c,d, also see Supporting Information (SI) Figure S1A). The deposition of a direct opal on the blade substrate (Figure 1c) resulted in a multi-domain, cracked colloidal crystal very similar to that grown on a flat surface. Even at the sharp 90° corners at the end of the blades, direct colloidal growth was often unaffected, with the crystal accommodating the sharp change in the nucleating surface via a disordered interface. The FFT image (Figure 1c inset) confirms that the crystal is disordered at this location (see smeared peaks).

In contrast, the co-assembled opal system (Figure 1d) consistently responded to the 90° shift by nucleating a different domain in the $\langle 100 \rangle$ orientation with respect to the growth direction in between the blade interfaces. This can also be seen in the FFT inset (Figure 1d), where the black hexagon highlights peaks corresponding to the predominant $\langle 110 \rangle$ direction (as in the unpatterned case) and the white

hexagon highlights peaks corresponding to the $\langle 100 \rangle$ direction of the newly-formed domains that formed between the ends of the blades.

The morphology of the colloidal film when it first begins to grow around blade structures (see SI, Figure S1B) indicates that the meniscus is pinned and distorted at the blade features during growth and that the colloids close-pack at the walls of the blades (see SI, Figure S1C). Similar close-packing behavior has been recently observed with direct 2D colloidal monolayers via the use of surface relief boundaries^[26] and has been attributed to meniscus pinning and consequent convective flow to the region.^[27] Another group noted that 3D direct opals pack into rectangular microchannels with the $[1\bar{1}0]$ crystalline direction oriented parallel to the walls of the channels,^[13c] yet failed to provide an explanation. We expect that in a defect-free FCC crystal, this observed close-packing of colloids along an imposed wall should nucleate a domain with a direction determined by the orientation of the wall (Figure 2a), thus allowing the geometry of the spatial constraint to fully control domain orientation. For example, if the nucleating surface is parallel to the growth direction of

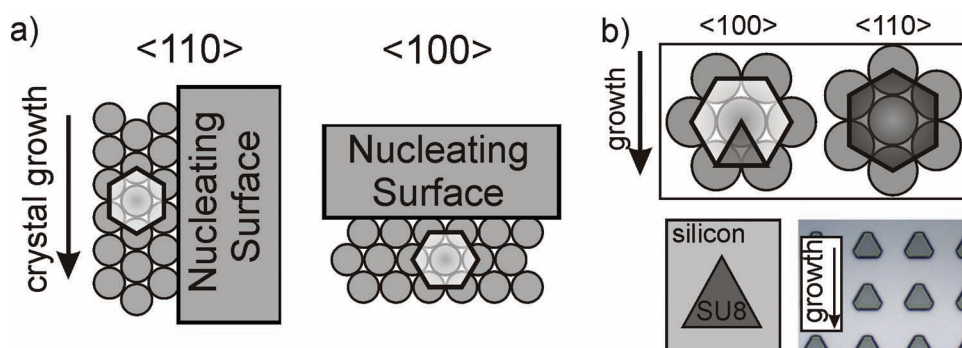


Figure 2. Schematic illustrating the nucleation behavior for defect-free colloidal crystals grown in response to differently oriented imposed constraints. a) A vertical wall constraint (left) would nucleate a $\langle 110 \rangle$ -oriented domain and horizontal wall (right) would nucleate a $\langle 100 \rangle$ -oriented domain with respect to the growth direction. b) A schematic shows that equilateral triangles or hexagons fit perfectly into a hexagonal colloidal crystal, and their orientation should determine the resulting crystal direction. While the orientation of hexagons shown on the right would correspond to the intrinsic $\langle 110 \rangle$ direction of inverse opals grown on the flat surface, the orientation of the triangles shown on the left is expected to rotate the crystallographic orientation of the inverse opal film by 90° to form a $\langle 100 \rangle$ -oriented crystal. An optical image of patterned equilateral triangles expected to nucleate $\langle 100 \rangle$ crystal domains is shown on the bottom right.

the crystal, it should result in the domain growth in the $\langle 110 \rangle$ orientation (with respect to the growth direction). If the surface is perpendicular to the growth, the domain should be in the $\langle 100 \rangle$ orientation. This shift in orientation from $\langle 110 \rangle$ to $\langle 100 \rangle$ is precisely what was observed for the assembly of the inverse opal around the 90° corners of the blade pattern (Figure 1d).

2.2. Nucleation of Large Single Crystals with Defined Orientation

The formation of large single crystals with controlled crystallographic orientation presents a significant challenge for the crystal growth community. Even more elusive is the ability to form hierarchically patterned single crystals. We anticipated that the nucleation behavior of inverse opal films that follow the orientation of the imposed walls can be extended to a larger scale, expanding the application possibilities of this method. In particular, in order to make geometrically-complex, hierarchical inverse opal structures with uniform crystallographic orientation, one needs a spatial constraint geometry that forces the nucleation of crystallographic domains to be consistent with the default hexagonal symmetry of colloidal crystals. One such geometry is an equilateral triangle whose in-plane rotation should determine the crystallographic orientation of the resulting crystal (Figure 2b). (Note that a hexagonal shape is also consistent with the symmetry of the crystal.)

To characterize the quality of the topographically templated colloidal crystals, they were imaged with an optical microscope by shining white light at a high angle of incidence onto the samples and capturing the scattered light with a microscope camera (Figure 3a). Using this approach we were able to probe the spectral variations in light scattering of domains shifted/rotated with respect to each other in the xy plane (not just capturing the rotations of domains with respect to the z -direction seen at normal incidence). The revealed structural

details are quite striking when one compares a film imaged under direct (0°) incidence versus one imaged at higher angle of light incidence (Figure 3b, also see SI Figure S2).

In order to test our previous hypothesis, direct and inverse opals were assembled around patterned equilateral, $2\text{ }\mu\text{m}$ -high SU8 triangles with $15\text{ }\mu\text{m}$ -long sides oriented for $\langle 100 \rangle$ growth, as shown in Figure 2b, left. As expected from the previous “blade” deposition example, the assembly of direct opals into such a configuration resulted in random defects and domains, as seen in the multi-colored titled optical image (Figure 3c). The inverse opal, however, remarkably reflected a single color on a large scale optical image, indicating that all the domains in the crystal have a uniform orientation (Figure 3d). SEM images of a typical area for both films (Figure 3e,f) verify these conclusions. The various domains of the direct opal are indicated and outlined on the SEM. An FFT image confirms the disordered crystallographic state of the film (Figure 3e). The inverse opal, on the other hand, appears to have a completely uniform crystallographic orientation, as confirmed by its FFT. The SEM image clearly shows that the resulting crystal is oriented in the $\langle 100 \rangle$ crystallographic direction, as controlled by the imposed orientation of the triangular walls. Interestingly, this orientation is 90° rotated from the preferential growth direction that inverse opals adopt on flat substrates (the $\langle 110 \rangle$ direction).

Thus, we have shown that spatial constraints can be designed to form patterned single crystals of inverse opals on a large scale and precisely control their crystallographic orientation, even if rotated away from the preferred growth direction of the crystal.

2.3. Nucleation of Altered Domains with Defined Location and Orientation

To further test the effect of crystallographically-compatible spatial constraints, an inverse opal was assembled into an array of $2\text{ }\mu\text{m}$ -high SU8 hexagons with $20\text{ }\mu\text{m}$ sides. While

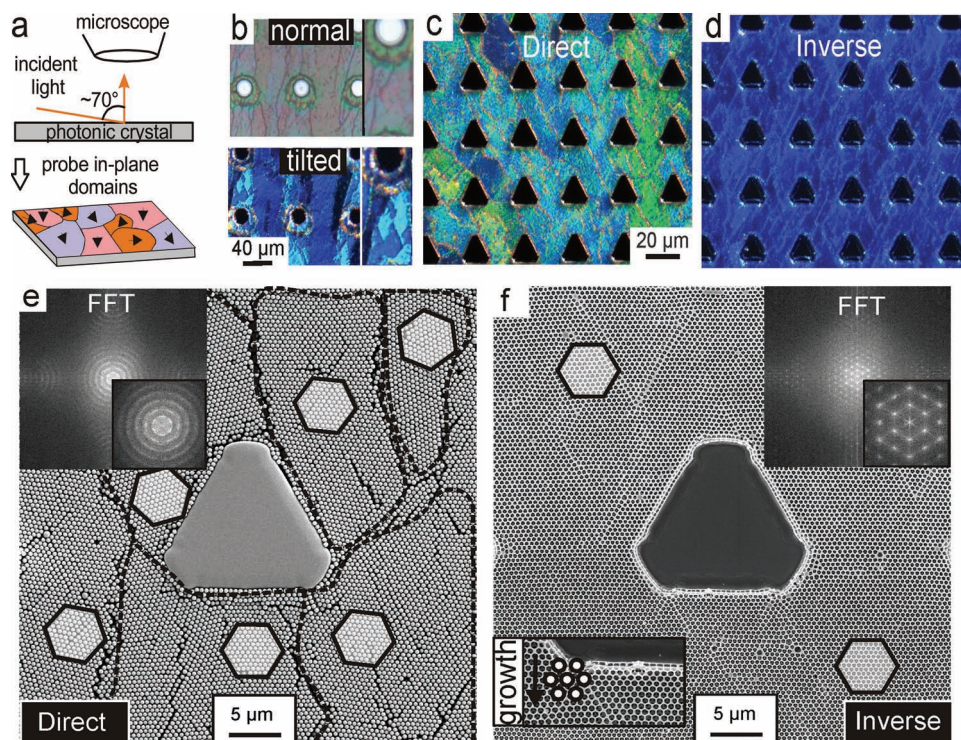


Figure 3. a) Schematic of the tilted optics setup. b) Characteristic reflected images of an inverse opal assembled around SU8 pillars taken with 0° (normal) incidence and with 70° tilted incidence. c,d) Tilted optical images of direct (c) and inverse (d) opals assembled around equilateral triangles. e,f) Enlarged SEM images of typical areas of a direct (e) and inverse (f) colloidal crystal surrounding a triangular feature. (Note: Organic SU8 features thermally decompose along with the sacrificial colloidal template in inverse opal synthesis.) The direct opal is not uniform, as shown by the FFT (inset), and is full of shifted domains outlined by dashed black lines (domain orientation is indicated by black hexagons). The inverse opal is remarkably uniform as shown by the FFT (inset). The growth direction is $\langle 100 \rangle$ (inset).

the hexagon geometry fits into the symmetry of the assembled opals, we intentionally designed the hexagons to have rounded, truncated corners, to disrupt the overall uniformity of the crystal orientation. The orientation of the walls of the hexagons was chosen to induce the $\langle 110 \rangle$ orientation of the colloidal crystal with respect to the growth direction

(Figure 4a inset). Indeed, the resulting opal shows a mostly uniform domain orientation, as seen by the predominance of one color in the optical images in Figure 4a. The SEM image of a typical region (Figure 4b) confirms that the major growth direction is $\langle 110 \rangle$ (large hexagons indicate domain orientation), again verifying that spatial constraint geometries

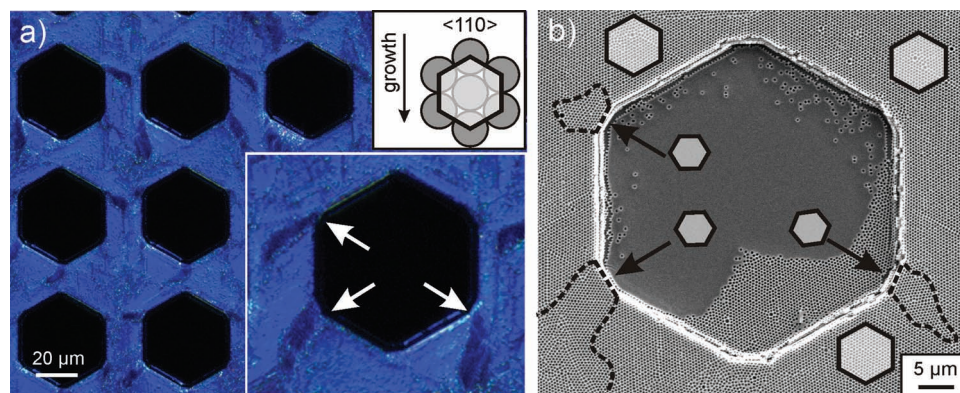


Figure 4. Nucleation of altered domains within largely uniform inverse opal films. a) Optical (tilted) images of an inverse opal film deposited around hexagonal prisms with truncated corners. The schematic (inset) shows how the orientation of the hexagons determines the resulting crystal direction. The darker colors in the optical images indicate the altered (rotated) domains that nucleated at the cropped corners of each hexagon (white arrows in inset). b) A typical SEM image shows that the predominant domain orientation (displayed with large black hexagons) is $\langle 110 \rangle$. Domains shifted in orientation from this main direction (small black hexagons) nucleated at the truncated corners of the hexagonal shape (indicated by black arrows). Boundaries of the altered domains are outlined in dashed black lines for clarity.

consistent with the hexagonal symmetry of colloidal crystals can be used to nucleate uniform inverse opal domains (as predicted in Figure 2b). However, though the tilted optics image of this film (Figure 4a) is dominated by one lighter color corresponding to the $\langle 110 \rangle$ orientation, there are regions in the image that are darker in color, indicating a different orientation. Due to the cropped corner design of the hexagons (Figure 4a,b, arrows), localized domains oriented away from the $\langle 110 \rangle$ direction have nucleated at these corners (small hexagons in Figure 4b). These differently oriented domains (outlined in Figure 4b) are finite in size because the crystal eventually corrects itself back to the dominant growth direction of $\langle 110 \rangle$, as dictated by the hexagon orientation.

This study confirms that properly designed spatial constraints not only enable the manipulation of inverse opal domain orientation on a large scale, but can induce the localized nucleation of finite domains of an altered orientation within a largely uniform film.

2.4. Control of Order, Disorder, and Quasi-Order in Assembled Opal Films

The demonstrated ability to induce local nucleation of altered domains at rounded corners of topographical features can be extended one step further to manipulate the order, polycrystallinity and size of crystalline domains. Because colloids close-pack around the walls of topographical patterns, a circular spatial constraint geometry is expected to produce nucleation of all possible domain orientations (i.e., disorder) in both direct and inverse opal systems, since it cannot be accommodated by the intrinsic hexagonal symmetry of the crystal. To test this hypothesis, surfaces bearing arrays of differently spaced 2 μm -high SU8 cylinders (4 μm in diameter) were used as templates for colloidal assembly. Closely spaced cylinders (Figure 5a,b, top row) led to the most disordered crystals. Direct assembly around these features (Figure 5a, top) resulted in disordered colloidal films that no longer maintained hexagonal symmetry even at short range, as also seen in the rings of the FFT (inset). Inverse opal assembly into the same pattern (Figure 5b, top) led to quasi-ordered films with a heavily distorted hexagonal lattice (see noisy, limited peaks of the FFT). With the cylindrical features spaced slightly further apart (second row of Figure 5a,b), polycrystalline

hexagonal domains of limited size began to appear in both direct and inverse opal systems (see FFT insets). Thus, the shape and spacing of imposed spatial constraints can be used to control the order and size of crystalline domains.

3. Discussion

In the present work we have demonstrated that topographically patterned templates with rationally designed 3D spatial constraints can be used to precisely control the crystallographic orientation, size, and crystal quality of inverse and direct opal domains. The case studies in this work illustrate the different levels of control that topographic patterning can impose on direct and inverse opals. Assembly into the rectangular blade pattern introduced the concept that inverse opal domain orientation can be locally controlled by spatial constraint geometry due to the colloidal close-packing around imposed nucleating walls and the increased interaction between adjoining colloids in this composite growth method. This nucleation control was also found to be scalable to produce large-area single crystalline films that assemble around features compatible with the hexagonal geometry intrinsic to colloidal systems, such as triangular or hexagonal prisms. Moreover, the former system provided the means to tune the crystallographic orientation of the single crystalline domains that follow the in-plane rotation of the imposed triangular features, thus forcing the crystals to grow in directions different from their intrinsic $\langle 110 \rangle$ crystallographic orientation observed on unpatterned substrates. We also showed it is possible to induce the localized nucleation of finite domains of an altered orientation within a largely uniformly oriented inverse opal film via assembly into an array of hexagonal prisms with truncated, and therefore differently-oriented edges. This effect was finally taken to the extreme, when a pattern of cylindrical features was used to manipulate disorder, quasi-order, polycrystallinity, and size of the ordered domains in inverse and direct opals by frustrating their hexagonal packing.

It appears that because co-assembly results in the increased interaction between adjoining colloids and fewer isolated defects in the crystal, this composite system generally allows for improved quality and control of the crystalline films as compared with direct opals. This type of topographic

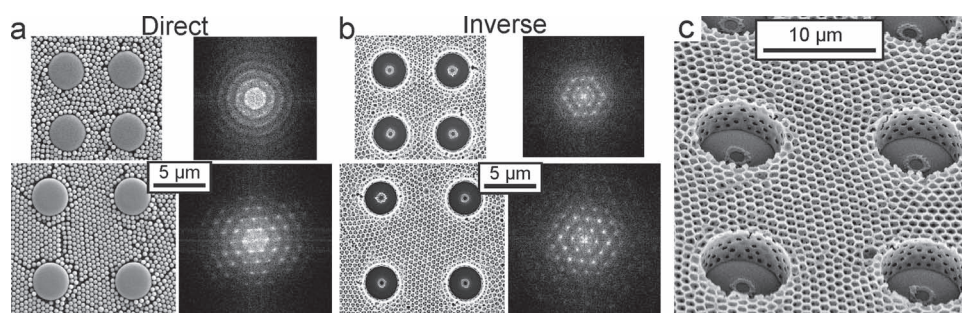


Figure 5. SEM images of direct and inverse opals assembled around cylindrical features. Arrays of circles allow for control of disorder, quasi-order and polycrystallinity (see FFT insets) and domain size in direct (a) and inverse (b) opals via constraint geometry and differences in feature spacing, leading to complex composite inverse opal structures (c).

co-assembly^[23] of inverse opals and the resulting all-silica 3D porous hierarchical structures (Figure 5c) would have been impossible with conventional production methods. The combination of these case studies lends insight into the types of parameters (shape, size, spacing of features) that need to be considered when topographical templates are used to manipulate and engineer the nucleation of direct and inverse opal films for the synthesis of complex, functional structures. In particular, we show that the optical properties of these complex structures are finely coupled to their crystallinity and defect distribution.

Control of crystal quality and order in colloidal structures is important in photonic systems, and has recently gained attention in the literature. Quasi-ordered (short-range order) and disordered photonic crystals are seen in numerous natural systems.^[28] The coloration in many species of birds is due to coherent scattering from layers of collagen fibers in avian skin^[29] and nanostructured keratin in feather barbs.^[30] The irregular lamellar structure in *Morpho* butterfly scales gives its wings a highly reflective and uniform blue color in a wide angular range^[31] and a disordered network of cuticular filaments in the scales of the *Cyphochilus* spp. beetle gives it the appearance of brilliant whiteness.^[32] Quasi-ordered photonic structures are also responsible for the colors seen on dragonflies^[33] and the weevil *Eupholus magnificus* beetle.^[34] Modeling of disordered and quasi-ordered structures has highlighted their possible applications in creating 2D^[35] and 3D^[36] photonic bandgap materials. Synthetic biomimetic approaches have also been adopted in order to simulate optical properties seen in natural systems. An amorphous 2D structure, fabricated with a top-down approach, was used to demonstrate control of lasing,^[37] while quasi-ordered and disordered 3D colloidal systems have been utilized to create angle-independent color arrays.^[38] Our topographical manipulation of the orientation, location, and crystalline order of photonic opal domains is closely related to these studies, and could provide an alternative, *bottom-up route* to the synthesis of a broad range of colloidal photonic systems with finely-tuned optical properties. Images from our tilted light source optical probe technique are an initial confirmation that we are indeed directing changes in the optical properties of these films.

4. Conclusion

We have described a bio-inspired bottom-up synthesis of multi-layered, colloidal crystal films formed directly on topographically patterned substrates via evaporative deposition of polymeric spheres with and without a silicate sol-gel precursor solution (to create inverse and direct opals, respectively). We demonstrated that colloidal self-assembly can be systematically studied and manipulated with rationally designed micrometer-scale topographical substrates to either form large patterned single crystals, or crystals with a fine-tuned extent of disorder, and to nucleate distinct colloidal domains of a defined size, location, and orientation in a wide range of length-scales. We believe that this method will increase the functionality of colloidal crystal materials, extending their applications as elements in optical circuits,

as tissue scaffolds, and as catalytic substrates. This work also explores the fundamental aspects of controlling colloidal crystal domain nucleation and growth, providing an important step forward in understanding the crystal growth and defect formation in colloidal systems.

5. Experimental Section

A flat or patterned silicon substrate (~1 cm × 4 cm), cleaned briefly under oxygen plasma (Diener Electric GmbH Femto-A plasma cleaner), was vertically suspended in a vial containing a 20 mL volume of 0.1% (by volume) colloidal solution in water. 450 nm diameter poly(methyl methacrylate) (PMMA) colloids in the suspension were synthesized via emulsion polymerization, using an ammonium persulfate initiator, and cleaned via centrifugation. For silica-colloid composite assembly, the solutions also contained 145 μ L of added hydrolyzed tetraethyl orthosilicate (TEOS) solution. The TEOS solution consisted of a 1:1:1.5 ratio by weight of TEOS (98% Aldrich), 0.10 M HCl, and ethanol (100%), respectively, stirred at room temperature for 1 h prior to use. The colloidal or colloid/TEOS suspension was allowed to evaporate slowly over a period of 1–3 days in a 65 °C oven on a pneumatic vibration-free table, to allow the deposition of a thin film onto the vertical substrate. For inverse opal synthesis, composite films were calcined in air at 500 °C for 5 h, with a 4 h ramp time (Thermo Scientific).

Patterned surfaces were prepared in two ways. The blade surface (see SI, Figure S1A) was fabricated using the Bosch process, as described elsewhere.^[39] The circular, hexagonal, and triangular features were patterned on a silicon wafer with SU8 using mask photolithography (Suss MJB4 Mask Aligner). The chrome masks were produced with the Heidelberg Mask Writer at the Center for Nanoscale Systems at Harvard University.

Optical images were taken using a custom upright optical Olympus microscope with the 20× or 50× objective. The samples were imaged in reflection with a fiber optic white light source (Cole Parmer 41723 series) tilted to have an incidence angle of ~70° with respect to the sample normal (Figure 3a). Films were also imaged by SEM (Zeiss Ultra or JEOL JSM 6390LV) at 5 kV after Pt/Pd-sputter coating. FFT (Fast Fourier Transform) image analysis was preformed via ImageJ.

Supporting Information

Supporting Information is available from the Wiley Online Library or from the author.

Acknowledgements

This work was supported by the Air Force Office of Scientific Research Award # FA9550-09-1-0669- DOD35CAP. L.M. acknowledges fellowship support from the Department of Homeland Security (DHS). M.K. acknowledges funding from the Alexander von Humboldt Foundation. Electron microscopy and photolithography were performed at Harvard's Center for Nanoscale Systems.

Fabrication was partially supported by the National Science Foundation's MRSEC Award #DMR-0820484. We thank Dr. Mughees Khan for nanofabrication of the blade surface used in this work.

- [1] a) H. A. Lowenstam, S. Weiner, *On Biomineralization*, Oxford Univ. Press, Oxford **1989**; b) C. C. Perry, T. Keeling-Tucker, *J. Biol. Inorg. Chem.* **2000**, *5*, 537–550; c) L. Addadi, S. Weiner, *Angew. Chem. Int. Ed.* **1992**, *31*, 153–169.
- [2] a) J. Aizenberg, D. A. Muller, J. L. Grazul, D. R. Hamann, *Science* **2003**, *299*, 1205–1208; b) N. B. J. Hetherington, A. N. Kulak, K. Sheard, F. C. Meldrum, *Langmuir* **2005**, *22*, 1955–1958; c) H. Li, H. L. Xin, D. A. Muller, L. A. Estroff, *Science* **2009**, *326*, 1244–1247; d) A. S. Finne, M. R. J. Scherer, R. Langford, S. Mahajan, S. Ludwigs, F. C. Meldrum, U. Steiner, *Adv. Mater.* **2009**, *21*, 3928–3932; e) C. Li, L. Qi, *Angew. Chem. Int. Ed.* **2008**, *47*, 2388–2393.
- [3] a) P. D. Yang, T. Deng, D. Y. Zhao, P. Y. Feng, D. Pine, B. F. Chmelka, G. M. Whitesides, G. D. Stucky, *Science* **1998**, *282*, 2244–2246; b) G. J. D. Soler-illia, C. Sanchez, B. Lebeau, J. Patarin, *Chem. Rev.* **2002**, *102*, 4093–4138.
- [4] N. V. Dziomkina, G. J. Vancso, *Soft Matter* **2005**, *1*, 265–265.
- [5] P. Schall, I. Cohen, D. A. Weitz, F. Spaepen, *Nature* **2006**, *440*, 319–323.
- [6] J. R. Savage, D. W. Blair, A. J. Levine, R. A. Guyer, A. D. Dinsmore, *Science* **2006**, *314*, 795–798.
- [7] P. Jiang, J. F. Bertone, K. S. Hwang, V. L. Colvin, *Chem. Mater.* **1999**, *11*, 2132–2140.
- [8] J. H. Holtz, S. A. Asher, *Nature* **1997**, *389*, 829–832.
- [9] I. Gourevich, H. Pham, J. E. N. Jonkman, E. Kumacheva, *Chem. Mater.* **2004**, *16*, 1472–1479.
- [10] a) E. Vekris, Y. Kitaev, D. D. Perovic, J. S. Aitchison, G. A. Ozin, *Adv. Mater.* **2008**, *20*, 1110–1116; b) O. D. Velev, A. M. Lenhoff, *Curr. Opin. Colloid Interface Sci.* **2000**, *5*, 56–63; c) M. S. Tirumkudulu, W. B. Russel, *Langmuir* **2005**, *21*, 4938–4948.
- [11] A. van Blaaderen, R. Ruel, P. Wiltzius, *Nature* **1997**, *385*, 321–324.
- [12] C. Jin, M. A. McLachlan, D. W. McComb, R. M. De La Rue, N. P. Johnson, *Nano Lett.* **2005**, *5*, 2646–2650.
- [13] a) Y. Xia, Y. Yin, Y. Lu, J. McLellan, *Adv. Funct. Mater.* **2003**, *13*, 907–918; b) G. A. Ozin, S. M. Yang, *Adv. Funct. Mater.* **2001**, *11*, 95–104; c) S. M. Yang, H. Míguez, G. A. Ozin, *Adv. Funct. Mater.* **2002**, *12*, 425–431; d) J. Xu, E. S. O'Keefe, C. C. Perry, *Mater. Lett.* **2004**, *58*, 3419–3423.
- [14] a) M. E. Davis, *Nature* **2002**, *417*, 813–821; b) L. J. Gibson, M. F. Ashby, *Cellular Solids*, Cambridge University Press, Cambridge, UK **1997**; c) O. M. Yaghi, H. L. Li, C. Davis, D. Richardson, T. L. Groy, *Acc. Chem. Res.* **1998**, *31*, 474–484; d) X. S. Zhao, F. B. Su, Q. F. Yan, W. P. Guo, X. Y. Bao, L. Lv, Z. C. Zhou, *J. Mater. Chem.* **2006**, *16*, 637–648.
- [15] J. Lee, S. Shanbhag, N. A. Kotov, *J. Mater. Chem.* **2006**, *16*, 3558–3564.
- [16] a) K. Lee, S. A. Asher, *J. Am. Chem. Soc.* **2000**, *122*, 9534–9537; b) I. B. Burgess, L. Mishchenko, B. D. Hatton, M. Kolbe, M. Lončar, J. Aizenberg, *J. Am. Chem. Soc.* **2011**, *133*, 12430–12432.
- [17] a) G. Q. Guan, R. Zapf, G. Kolb, V. Hessel, H. Lowe, J. H. Ye, R. Zentel, *Int. J. Hydrogen Energy* **2008**, *33*, 797–801; b) M. M. Ren, R. Ravikrishna, K. T. Valsaraj, *Environ. Sci. Technol.* **2006**, *40*, 7029–7033.
- [18] a) V. L. Colvin, *MRS Bull.* **2001**, *26*, 637–641; b) J. C. Lytle, A. Stein, *Ann. Rev. Nano Res.* **2006**, *1*, 1–79; c) A. Stein, R. C. Schroden, *Curr. Opin. Solid State Mater. Sci.* **2001**, *5*, 553–564; d) Y. Xia, B. Gates, Y. Yin, Y. Lu, *Adv. Mater.* **2000**, *12*, 693–713.
- [19] a) B. T. Holland, C. F. Blanford, A. Stein, *Science* **1998**, *281*, 538–540; b) O. D. Velev, T. A. Jede, R. F. Lobo, A. M. Lenhoff, *Nature* **1997**, *389*, 447–448.
- [20] Z. Gu, A. Fujishima, O. Sato, *Chem. Mater.* **2002**, *14*, 760–765.
- [21] a) A. Blanco, E. Chomski, S. Grachtchak, M. Ibsate, S. John, S. W. Leonard, C. Lopez, F. Meseguer, H. Miguez, J. P. Mondia, G. A. Ozin, O. Toader, H. M. van Driel, *Nature* **2000**, *405*, 437–440; b) J. S. King, D. Heineman, E. Graungard, C. J. Summers, *Appl. Surf. Sci.* **2005**, *244*, 511–516; c) M. Scharer, X. Wu, A. Yamilov, H. Cao, R. P. H. Chang, *Appl. Phys. Lett.* **2005**, *86*, 151113–151115.
- [22] a) N. Tétreault, A. Mihi, H. Míguez, I. Rodríguez, G. A. Ozin, F. Meseguer, V. Kitaev, *Adv. Mater.* **2004**, *16*, 346–349; b) S. A. Rennie, F. Garcia-Santamaria, P. V. Braun, *Nat. Photonics* **2007**, *2*, 52–56; c) L. Wang, Q. Yan, X. S. Zhao, *Langmuir* **2006**, *22*, 3481–3484.
- [23] B. Hatton, L. Mishchenko, S. Davis, K. H. Sandhage, J. Aizenberg, *Proc. Natl. Acad. Sci. U. S. A.* **2010**, *107*, 10354–10359.
- [24] M. Ishii, M. Harada, H. Nakamura, *Soft Matter* **2007**, *3*, 872–872.
- [25] K. Wostyn, Y. Zhao, B. Yee, K. Clays, A. Persoons, G. de Schaetzen, L. Hellemans, *J. Chem. Phys.* **2003**, *118*, 10752–10752.
- [26] E. C. H. Ng, K. M. Chin, C. C. Wong, *Langmuir* **2011**, *27*, 2244–2249.
- [27] a) N. D. Denkov, O. D. Velev, P. A. Kralchevsky, I. B. Ivanov, H. Yoshimura, K. Nagayama, *Nature* **1993**, *361*, 26–26; b) A. S. Dimitrov, K. Nagayama, *Langmuir* **1996**, *12*, 1303–1311; c) E. Adachi, A. S. Dimitrov, K. Nagayama, *Langmuir* **1995**, *11*, 1057–1060.
- [28] P. Vukusic, D. G. Stavenga, *J. R. Soc. Interface* **2009**, *6*, S133–S148–S133–S148.
- [29] R. O. Prum, R. Torres, *J. Exp. Biol.* **2003**, *206*, 2409–2429.
- [30] R. O. Prum, R. H. Torres, S. Williamson, J. Dyck, *Nature* **1998**, *396*, 28–29.
- [31] S. Kinoshita, S. Yoshioka, K. Kawagoe, *Proc. R. Soc. London, Ser. B* **2002**, *269*, 1417–1421.
- [32] P. Vukusic, B. Hallam, J. Noyes, *Science* **2007**, *315*, 348–348.
- [33] R. O. Prum, J. A. Cole, R. H. Torres, *J. Exp. Biol.* **2004**, *207*, 3999–4009.
- [34] C. Pouya, D. G. Stavenga, P. Vukusic, *Opt. Express* **2011**, *19*, 11355–11364.
- [35] a) C. Jin, X. Meng, B. Cheng, Z. Li, D. Zhang, *Phys. Rev. B* **2001**, *63*, 195107–195107; b) M. Florescu, S. Torquato, P. J. Steinhardt, *Proc. Natl. Acad. Sci. U. S. A.* **2009**, *106*, 20658–20663.
- [36] K. Edagawa, S. Kanoko, M. Notomi, *Phys. Rev. Lett.* **2008**, *100*, 013901–013901.
- [37] H. Noh, J.-K. Yang, S. F. Liew, M. J. Roops, G. S. Solomon, H. Cao, *Phys. Rev. Lett.* **2011**, *106*, 183901–183901.
- [38] a) J. D. Forster, H. Noh, S. F. Liew, V. Saranathan, C. F. Schreck, L. Yang, J.-G. Park, R. O. Prum, C. S. O'Hern, S. G. J. Mochrie, H. Cao, E. R. Dufresne, *Adv. Mater.* **2010**, *22*, 2939–2944; b) K. Ueno, A. Inaba, Y. Sano, M. Kondoh, M. Watanabe, *Chem. Commun.* **2009**, 3603–3605; c) M. Harun-Ur-Rashid, A. Bin Imran, T. Seki, M. Ishii, H. Nakamura, Y. Takeoka, *ChemPhysChem* **2010**, *11*, 579–583; d) I. Lee, D. Kim, J. Kal, H. Baek, D. Kwak, D. Go, E. Kim, C. Kang, J. Chung, Y. Jang, S. Ji, J. Joo, Y. Kang, *Adv. Mater.* **2010**, *22*, 4973–4977.
- [39] T. N. Krupenkin, J. A. Taylor, E. N. Wang, P. Kolodner, M. Hodes, T. R. Salamon, *Langmuir* **2007**, *23*, 9128–9133.

Received: December 21, 2011
 Published online: March 28, 2012